Commercial Magnetic Sensors (Hall and Anisotropic Magnetoresistors)

Michael J. Haji-Sheikh

1 Introduction

Magnetic sensors account for a significant portion of the sensing market. Manufactures such as Honeywell, Phillips, Optek, Cherry, and Infineon primarily make commercial and automotive sensors while Fujitsu, IBM, Maxtor and Seagate control the information sector additionally Asahi Chemicals has a significant position in fan speed sensing. There are two types of magnetic sensors. The first type of magnetic sensor commonly used is the Hall-effect sensor. The Hall-effect sensor is a device that depends on the mobility of carriers in a semiconductor material such as silicon. The second type of magnetic sensor is the magnetoresistor. Magnetoresistors come in different types. These are ordinary magnetoresistors (MR), anisotropic magnetoresistors (AMR), giant magnetoresistors (GMR) and colossal magnetoresistors (CMR). Of these, the CMR has yet to move out of the research phase. These commercial devices, manufactured by the above companies, have diverse applications such as proximity sensors, gear-tooth sensors, and read head sensors. An example of how important the magnetic sensor is, a search of the United States Patent Data Base shows over three thousand patents using hall-elements. Additionally there are over four hundred patents using magnetoresistors. There is an art and a science to building commercial sensors. Often it takes a diverse group of scientists and engineers to characterize and model these sensors prior to committing a design to production. This is due to the secondary nature of the sensing mechanisms which are commonly used. Most sensing mechanisms only show up as small perturbations in a larger property such as resistivity or permitivity. Often these perturbations are only a few percent of a typical full scale output for a given sensor. The difficulty in using these properties as sensing mechanisms is that they often interact with their surroundings in ways which obscure the measurements of interest. What is meant with this statement is that the structures often use to mount the sensors will have just as much influence as the external signal as the output of the sensor.

Michael J. Haji-Sheikh
Associate Professor of Electrical Engineering, College of Engineering and Engineering Technology, Northern Illinois University, De Kalb Illinois 60115. e-mail: mhsheikh@ceet.niu.edu

S.C. Mukhopadhyay, R.Y.-M. Huang (eds.), *Sensors*,

Nanotechnology related advances will effect how we view and develop a new generation of sensors. The interaction of magnetic materials and the patterning of these materials will eventually lead to devices that we have not yet conceived. Most magnetic thin film devices are nanoscale in the thickness but newer research areas include nanoscale patterning and nanoscale self-assembly.

2 Hall Sensor Design

The design of Hall-effect sensors has been well detailed in Popovic's book [1] so we will only lightly treat the physics and concentrate on the procedures required to build a production sensor. The design of Hall-effect sensors is an exercise in geometry and device physics. The typical Hall-effect sensor, or Hall cell, is built into a lightly doped n-type epitaxial layer due to the high electron mobility. The classical mechanics of the Hall-effect depends on the Lorentz force. The Lorentz force states that there is a force placed by a magnetic field onto a moving charged particle. The Lorentz equation is

$$\vec{F}_m = -q(\vec{v} \times \vec{B}), \tag{1}$$

where F_m is the Lorentz force, q is the charge on an electron, v is the electron velocity, and Bis the external magnetic field. A simple schematic of a Hall cell is shown in Fig. 1. The magnetic field is normal to the top surface. The electric field set up by this external magnetic field. There is a counter-balancing electric field which is

$$\vec{E}_h = -\vec{v} \times \vec{B} \tag{2}$$

set up when the magnetic field is applied.

The hall voltage set up at the side taps is

$$V_h = \int_m^n \vec{E}_H \bullet \mathrm{d}\vec{z} \tag{3}$$

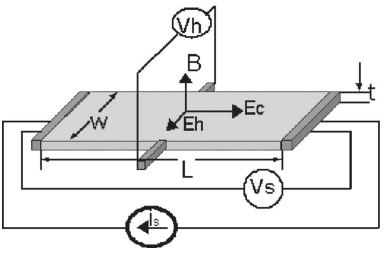

Fig. 1 Schematic of a rectangular Hall-effect element

and as defined in Popovic [1]

$$V_{hp} = \mu_p E_x B_y w \tag{4}$$

and

$$V_{hn} = \mu_p E_x B_y w \tag{5}$$

for the p-material and the n-material respectively. Additionally, the Hall electric field is

$$\vec{E}_H = -R_H(\vec{J} \times \vec{B}) \tag{6}$$

where the Hall Coefficient R_H for p-material and n-material is

$$R_{Hp} = 1/qp \quad R_{Hn} = 1/qn \tag{7}$$

where p is the number of p-carriers per cubic centimeter in the semiconductor and n is the number of n-carriers per cubic centimeter in the semiconductor. The hall voltage can be rewritten

$$V_{hp} = \frac{R_H}{t} I\, B_\perp \tag{8}$$

where I is the source current, t is the Hall cell thickness and B is the perpendicular magnetic field. For finite contact Hall cells

$$V_{hp} = G\frac{R_H}{t} I\, B_\perp \tag{9}$$

where G is a geometrical correction factor. The most common design for the for commercial Hall-effect sensor is euphemistically called the 'band-aid' contact Hall. Fig. 2 is a schematic of a 'band-aid' device. The name 'band-aid' comes from the resemblance of the contact to the medical gauze.

To effectively manufacture and calibrate a Hall-effect sensor, it requires an integrated manufacturing concept. These sensors required to have a high degree of manufacturing accuracy and a high degree measurement accuracy. This is accuracy

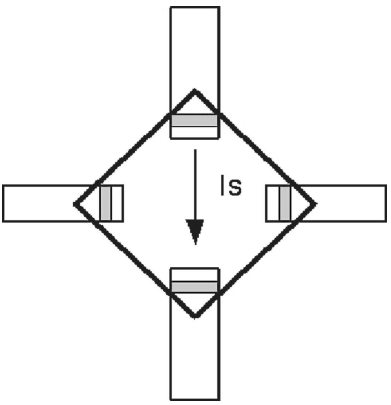

Fig. 2 The 'band-aid' hall cell. It comprises of a n-epitaxial area with a high concentration n-contact area and metal interconnect. This cell is demonstrated without a field plate

is important, since many of the applications are critical for system functionality. An important issue for the Hall-effect sensor in the effect of piezoresistance on the offsets. There are many methodologies for the balancing out the stress effects on the Hall-effect sensor. These stress balancing methods must be applied in the concept stage. These range from using (100) silicon to using dual and quad Hall cells. An important resource for research of the Hall-element is the United States Patent Office database. This resource is free and is not only able to be searched by the www.uspto.gov search engine but also is open to searches by popular commercial search engines.

One of the more recent innovations in Hall devices is the use of field plates to adjust offsets. Cohen [2] extends the patent by Plagens [3], which proposes to use metal or polygates placed in critical positions on the field oxide. These gates modulate the resistivity at the surface of the Hall-element to throw in a counter-offset.

Alexander's [4] patent uses a temperature compensated power supply to hold the offset constant which is a more standard method in sensing. Steiner et al. [5] looks at a more novel method of Hall-element design. The first 3 patents [2, 3] deal with traditional rectangular hall elements whereas Steiner deals with a circular element and spins the current in a circle to subtract the offset.

The traditional way to correct offsets is the addition of Hall-elements with currents running in multiple paths. The dual Hall cell has current running at ninety degrees to each other to neutralize the stress offsets due to piezoresistance effects. This though, increases the current required by a factor of two. The quad Hall shown in Fig. 3 not only balances out the stress induced offsets but additionally removes alignment induced offsets. The unfortunate side effect is that the quad hall cell has four times the current of the single hall cell.

The location of the Hall cell in the chip i.e. whether the sensor is on the edge of the chip versus the center can also effect the signal to mechanical noise ratio. With the introduction of digital technologies, the use of CMOS switches allows for the electrical rotation of the supply and sense leads to minimize the stress effects. The switches used for these type of sensors have to have a significantly large enough area so as to minimize the on-resistance. The Steiner patent [5] is representative of the offset adjustment methodology. Another invention that has affected how Hall-effect sensors are designed is the chopped Hall sensor which was invented by Bilotti [7] as shown in Fig. 5. Unlike the Steiner patent, the current is not rotated to all four possible positions but to two positions, ninety degrees apart.

To minimize packaging stresses, not only should the layout of the chip be considered but the layout of the package and chip both should be considered for a complete design pictures. The total stresses of the mounting on the die attach flag plus the over molding will effect the offsets of the Hall-effect sensor. As stated earlier, the offsets generated by the packaging stresses cannot be separated from the signal of interest. There are subtle effects of die coatings which can also effect stress induced offsets due to over molding. The proposed method of designing a Hall-effect

sensor, or any sensor, is to combine modeling with experimental verification. It is important to test and calibrate any model using some form of test structures. This calibration will pay off in the long run since it allows the designer to perform software designs of experiment (or DOE). These software experiments allow for a rapid minimization of the design options and design cycles. Due to the fact that Hall-effect devices are generally in *n*-type silicon (due to the significantly higher mobility), the piezoresistance coefficients of *n*-type silicon need to be obtained. The definition of piezoresistance is the change in the resistance of a material with an induced strain. The work of Matsuda et al. [8] details the piezoresistance mechanisms and coefficients for *n*-type silicon. The tensor relationship using both first and second order effects are

$$\frac{\partial \rho}{\rho_o} = \sum_j \pi_{ij} T_j + \sum_{j,k} \pi_{ijk} T_j T_k \tag{10}$$

where T is the stress $\partial\rho/\rho_o$ is the normalized resistance and π_{ij} is the first order piezoresistance coefficient and π_{ijk} is the second order coefficient. This equation in combination with a finite element analysis program such as ANSYS will allow for the calculation of voltage offsets generated by packaging stresses. Additionally a detailed graphical analysis was done by Kanda [9] in 1982. Once the best possible candidates for a particular application are chosen, then a test structure layout is made using the modeled design. The tests structures are then manufactured in the particular technology i.e. CMOS or Bipolar. After the silicon is finished, the measurement and evaluation starts.

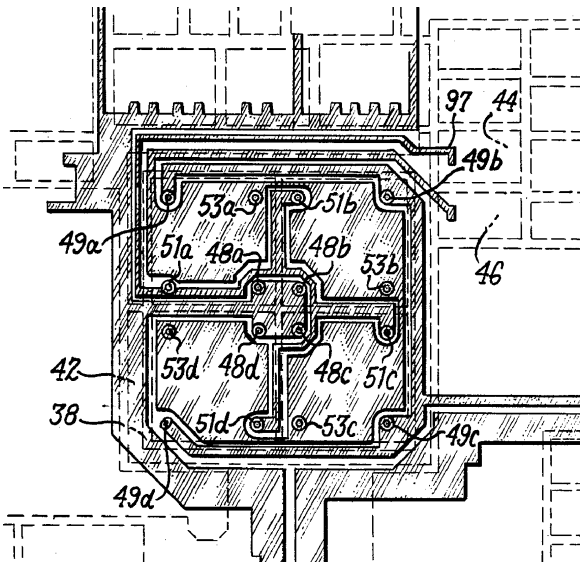

Fig. 3 Quad Hall cell with the supply voltage in the center of the cell. This patented method of quad-hall cell was invented by Higgs and Humenick [6]

3 AMR (Anisotropic Magneto-Resistive) Sensors

There are many different magnetic field sensing applications. Unfortunately, Hall sensors cannot cover all these applications. Magnetoresistive sensors for these applications offer higher sensitivities and superior performance. These applications range from engine position sensing to hard drive read heads. Newer AMR read heads are often combined with GMR sensors to help increase the aerial density. Additional applications range from proximity sensing to wheel speed detection.

There are many inventions based on magnetoresistivity. One of the first sensors in the U.S. Patent files is Nepela and Potter [10] and Lee's [11]. Potter [12] is also the author of one of the first comprehensive papers on the magnetoresistive effect in the general literature. These devices used the properties inherent in magnetoresistance to read recorded data from a magnetic storage media. This concept moved from the analog recording industry to data storage over the following years. A picture of the Lee's [11] invention is shown in Fig. 4. This sensor requires a field of ninety degrees to the direction of the serpentine section in the center.

The history of the magnetic recording using AMR sensors can be shown in the history of applicable inventions [13, 14, 15, 16, 17, 18]. Recent work in the recording and read head area has focused more on GMR than AMR. Industrial and automotive applications for AMR sensors range from proximity sensors to rotational speed sensors. Initially, AMR sensors were used as sensitive magnetometers as shown by Paul et al. [19], but now have been shown to be much more useful and flexible. One application that has recently come into its own is the magnetic rotary encoder.

One of the first recorded invention of this type is the rotary encoder invented by Ito et al. [20] and shown in shown in Fig. 5. This concept is expanded on by Haji-Sheikh et al. [21] to determine both speed and direction and is shown in Fig 6. Previous approaches for AMR models approach magnetoresistance in a relatively piecewise manner [22]. The normal procedure for design of magnetoresistors outlined in Tummanski [23] have not changed significantly since the mid-eighties and can be difficult to use. The design equations require fixing the field angle to resistor direction which means that the user must have multiple design equations. There are no above saturation models for sensor design, until recently, that accurately model a sensor element. The method presented here is an approach which

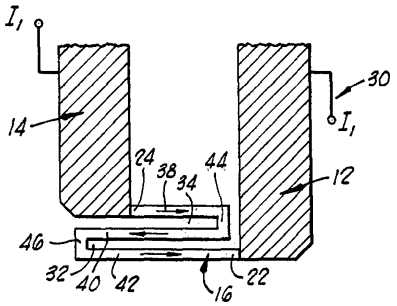

Fig. 4 Early invention showing the primary sensing element in F. Lee's [11] patent

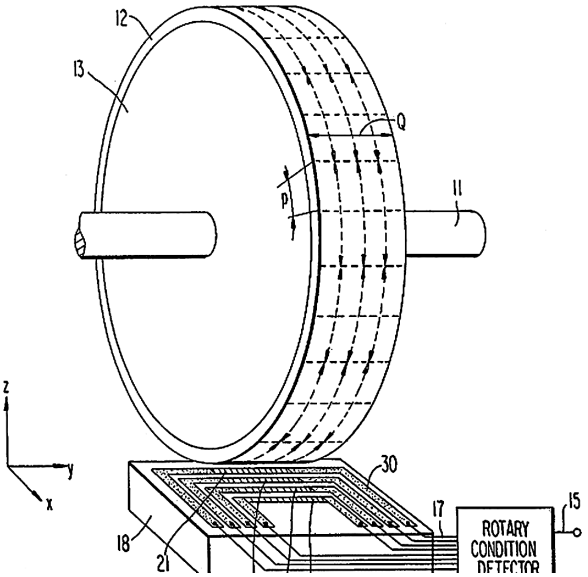

Fig. 5 Magnetic rotary encoder schematic from Ito et al. [20]

has been successfully used for applications ranging from a high current sensor to wheel-speed sensors which use saturation mode magnetoresistors.

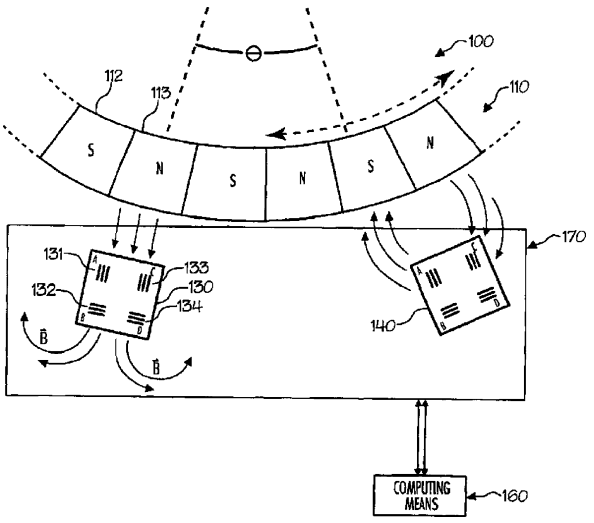

Fig. 6 Magnetic encoder using two sensors to be able to determine speed and direction of a ring magnet from Haji-Sheikh et al. [21]

4 AMR Model

AMR sensors can be used in two basic modes i.e. above magnetic saturation and below magnetic saturation. The curve shown in Fig. 7 shows the response of a anisotropic magnetic resistor with a transverse magnetic field. This figure breaks up the model into the above saturation value and the below saturation value. To understand the total behavior of the magnetoresistor, it is important to understand the behavior of the magnetoresistor in saturation. Since the above saturation resistivity is purely angle dependent, this model should be done first and then used to model sub-saturation behavior. To generate model information, test samples of Kelvin connected magnetoresistors need to be made at specified widths and thicknesses so as to sample the possible design space. Figure 8 is a schematic of a Kelvin connected resistor with the current in the outer connections and the voltage measure in the inside connections. To characterize the AMR film, it is important to understand some of the material properties of the film itself. The most common method of production of both anisotropic magnetoresistive films is by the use of plasma deposited materials. The films used to make the AMR sensors are oriented generally on the (111) plane and can be modeled as a single domain film.

To evaluate the crystallite orientation, samples were taken to Argonne National Laboratories Advanced Photon Source. Figures 9 and 10 are the results of zone plate measurements. The results show that the initial permalloy deposition aligns with the TaN (111) then the NiFe (111) increases in intensity with thickness. This increasing intensity demonstrates that the permalloy films are strongly (111) oriented. This matches data generated by Yeh [24] where he demonstrates the strength of the film orientation depending on the seeding layer.

The films deposited by Yeh [24] on SiO_2 were weakly oriented whereas the films deposited on Si_3N_4 and TaN were strongly oriented. The exact mechanisms of magnetoresistance is well beyond the scope of this analysis though an interesting paper

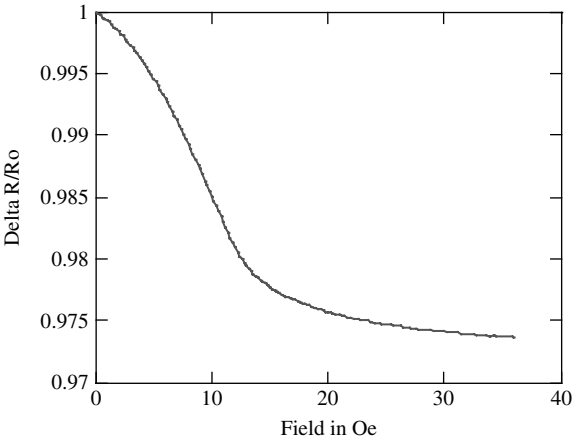

Fig. 7 The transverse magnetoresistance curve for a 37.5 nm thick magnetoresistor with a 35 μm wide resistor

Fig. 8 Kelvin connected magnetoresistor

by Berger [25] was performed to determine the mechanisms of magnetoresistance. Berger's experiment analyzed the saturation value of magnetoresistance as it is related to crystal orientation. Berger's experiment took three single crystal nickel resistors (100,110,111) and oriented them so that the resistor was ninety degrees to the magnetic field direction. Notably the (111) oriented single crystal nickel sample showed no magnetoresistance variation as the sample was rotated so that the maximum change stayed constant. Berger assumed that his measurement were not accurate enough to sense the resistance variation in the six fold symmetry plane. This could explain some of the single domain behavior of the permalloy film.

Historically, all analysis of magnetoresistance has started with the Voigt-Thompson equation [25, 26]

$$\frac{\Delta R}{R_o} = \frac{\Delta R_{\max}}{R_o} \cos^2 \theta. \tag{11}$$

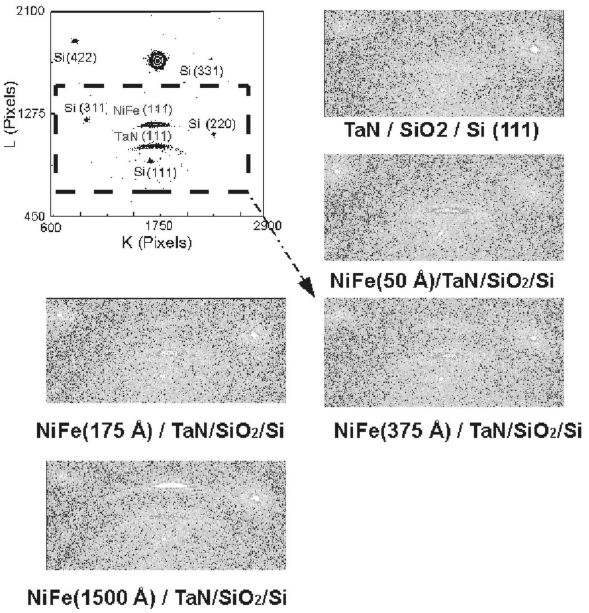

Fig. 9 Synchrotron x-ray reciprocal mapping of permalloy thin films using an image plate. Courtesy of Y. Yoo taken at Argonne National Labs

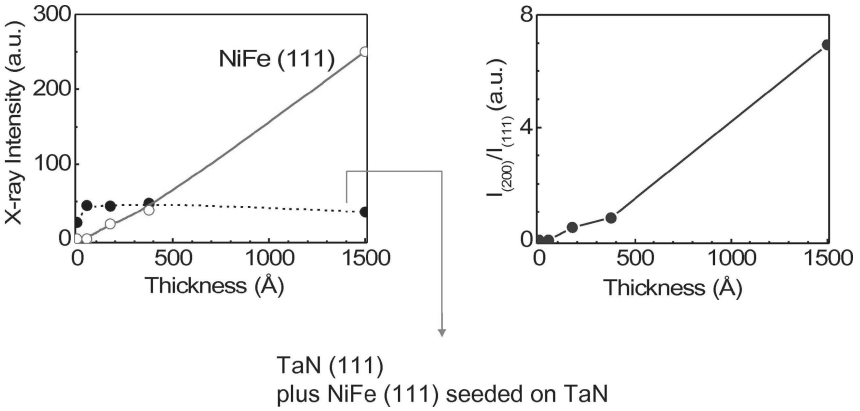

Fig. 10 Plot of x-ray intensity versus film thickness for a TaN/NiFe film. Courtesy of Y. Yoo taken at Argonne National Labs

Unfortunately, this relationship does not match the behavior of strongly oriented magnetoresistive films. To determine the saturated resistor behavior it is necessary to apply the basic tensor relationships as outlined in Nye [27]. This model can then be used to model the effect of a transverse applied field on the AMR of individual sensor elements. The results of solving the minimum energy equation (2) results in (12),

$$\Delta\theta = \frac{MH}{2K_u}\cos\theta, \tag{12}$$

where M is the magnetization, H is the external field, and K_u is the anisotropy constant. This change in angle can be used to calculate the change in resistance for a given applied field. To solve for the magnetoresistance of a thin film, it is necessary to set the proper initial conditions. Initial conditions for the AMR effect often assume that the resistance is completely anisotropic and that there are no isotropic scattering centers, This truly cannot be the case so a modified version of these initial conditions are as follows,

$$\rho\|' = \rho\| + \rho_o \tag{13}$$

$$\rho\perp' = \rho\perp + \rho_o \tag{14}$$

$$\Delta\rho' = \frac{\rho\|' - \rho\perp'}{2}, \tag{15a}$$

$$\rho' = \frac{\rho\|' + \rho\perp'}{2}, \tag{15b}$$

where the resistivities are related to the magnetization and ρ_o is the isotropic resistivity. Isotropic resistivity has many contributors such as grain boundaries and other conduction electrons. From equations (13)–(15b) the following tensor relationship can be defined,

$$P'_{\text{total}} = P'_o + P'_m, \tag{16}$$

where P'_m is the magnetic portion of the resistivity, P_0 is the isotropic portion and the total is now

$$\mathrm{P}'_{\text{total}} = \begin{bmatrix} \rho_0 & 0 \\ 0 & \rho_0 \end{bmatrix} + \begin{bmatrix} \rho' + \Delta\rho' \cos(2\theta) & \Delta\rho' \sin(2\theta) \\ \Delta\rho' \sin(2\theta) & \rho' - \Delta\rho' \cos(2\theta) \end{bmatrix} \tag{17}$$

By solving the following relationship,

$$\vec{E} = \rho\vec{J} \tag{18}$$

where E is the electric field and J is the current density. The modified AMR relationship can be shown to be similar to the Mohr's circle as described in Nye [27] and is as shown in (19),

$$\rho_{\text{eff}} = \rho_o + \rho' \left[\left(1 + \tfrac{\Delta\rho'}{\rho'} \cos 2\theta \right)^2 + \left(\tfrac{\Delta\rho'}{\rho'} \sin 2\theta \right)^2 \right]^{\frac{1}{2}} \tag{19}$$

This derivation of this equation is detailed in Haji-Sheikh et al. [28]. Equation (19) cannot be calculated directly but the data can be arrived at by an equivalent voltage form. The equation shown in (20) is the measurable form for which the AMR data can be fit,

$$V_{\text{total}} = I_s R_o \left(A + B \left((1 + C\cos 2\theta)^2 + (C \sin 2\theta)^2 \right)^{\frac{1}{2}} \right). \tag{20}$$

To develop an accurate AMR relationship, it is important to make detailed measurements of magnetoresistance versus magnetization angle. This measurement is best done using purely electrical methods since mechanical methods can have significant issues with lash. Screw lash is a mechanical hysteresis which is difficult to overcome and creates an inaccuracy in the rotation angle measurement in the mechanically positioned measurement systems. Alternately, inaccuracies using electrical methods can be as small as a few hundredths of a percent. The development of a measurement system which can apply magnetic field angles carefully and accurately is a critical step. This starts with using a wafer prober which is made from non-magnetic materials then designing an x–y Helmholtz coil which can apply at least 30 Oe in each direction. Unfortunately, to make such a system some mechanical jigging is necessary to align precise right angles.

$$\vec{B} = \vec{a}_z \frac{\mu_o I b^2}{2\left(z^2 + b^2\right)^{\frac{3}{2}}} \tag{21}$$

and

$$\vec{B} = \vec{a}_z \frac{N\mu_o I b^2}{2\left(z^2 + b^2\right)^{\frac{3}{2}}} \tag{22}$$

for a Helmholtz coil with multiple wraps. The magnetic field is calculated from equation (22) where N is the number of turns per coil, I is the current, z is the halfway point between the coils, b is the radius of the coils and μ_o is the permeability

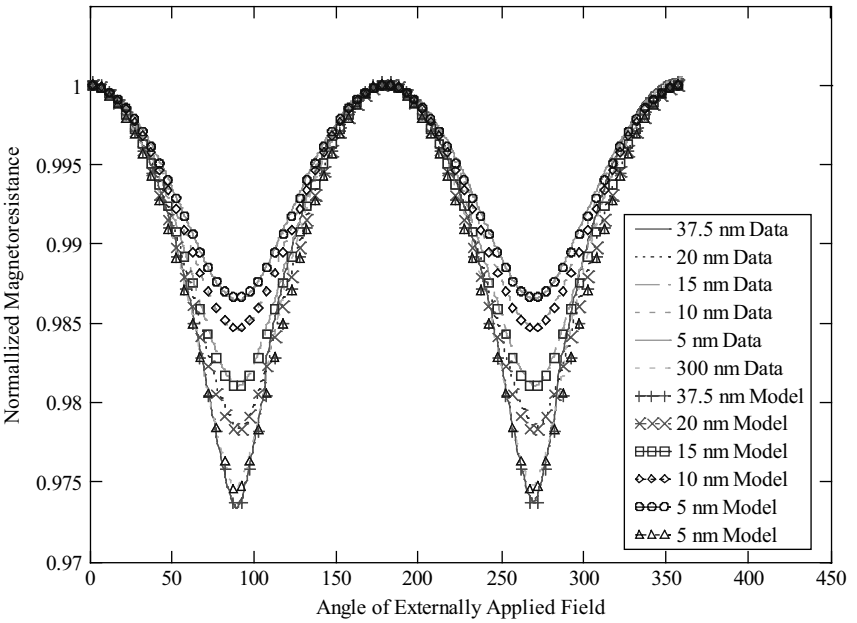

Fig. 11 Magnetoresistance versus angle for individual AMR resistors. This demonstrates the rhombehedral tensor model against the actual data. The model shown in this plot is necessary to extract the angle of magnetization rotation for a given hard axis field [28]

of free space (a permeable pole piece is undesirable due to the remnant field effect). The farther away the coil from the test structure and the larger the coil the higher the current and or the more coils necessary. The more wraps the more wire the higher the resistance in the coil itself which in turn increases the voltage and the temperature. The test temperature needs to be closely monitored due to the high temperature coefficient of resistivity of the permalloy material. Test results, in saturation, of a TaN/NiFe film used in commercial sensing is shown in Fig. 11. The data was taken using an automated test system which was programmed to rotate the field in the horizontal plane. The tensor model shown here can accurately track the resistance as the magnetization angle is rotated. Table 1 shows the coefficients used to fit the resistances plotted in Figure 11. It is apparent that the magnitude of the resistance change varies with the thickness of the film. Not only does the magnitude change but the shape of the curve changes. The *C* coefficient tracks the shape of the resistance

Table 1 Table of coefficients of fit calculated for the graph in Fig. 11

	5.0 nm	10.0 nm	15.0 nm	20.0 nm	25.0 nm	30.0 nm	37.5 nm
A	.97923	.97580	.97340	97090	.97050	.96968	.97000
B	.01420	.01640	.01695	.01695	.01726	.01722	.01630
C	.47647	.47700	.57200	.57200	.71800	.76944	.84500

rather than the magnitude. The value of C increases with thickness which leads to one to make the next logical extension. If C is equal to one the equation reduces to,

$$\rho_m = \rho\|' * |\cos\theta| \tag{23}$$

which is an interesting result. This result seams to verify the lack of magnetoresistance variation in the (111) which was noted by Berger [25]. The results of the preceding analysis have been applied to a Wheatstone bridge sensor (shown in Fig. 12) against a forty-eight pole-pair ring magnet. A forty-eight pole pair magnet is a composite magnet which has alternating magnetic poles. A ring magnet is the same 48 pole pairs in a ring drive off of a shaft (or spindle).

The bridge is two voltage dividers in parallel and can be solved by the following relationship

$$\Delta V = V_0 \frac{R_2}{R_2 + R_1} - V_0 \frac{R_4}{R_3 + R_4} \tag{24}$$

and

$$R_1 + R_2 = R_3 + R_4 \tag{25}$$

so

$$\Delta V = V_o \frac{R_2 - R_4}{R_2 + R_1}. \tag{26}$$

Each of the individual resistor elements has the same nominal resistance so that the resistors can be represented by

$$R_1 = R_o\left(A + B\left((1 + C\cos 2\theta)^2 + (C\sin 2\theta)^2\right)^{\frac{1}{2}}\right) \tag{27}$$

$$R_1 = R_o\left(A + B\left((1 + C\cos 2(\theta + 90^o))^2 + (C\sin 2(\theta + 90^o))^2\right)^{\frac{1}{2}}\right) \tag{28}$$

$$R_2 = R_3 \tag{29}$$

$$R_1 = R_4 \tag{30}$$

Replacing the individual resistors with the above equations creates a sensor bridge whose output is dependent on the angle of the external field. An important concept in magnetoresistance is the idea of hard-axis and easy-axis film behavior. Figure 12 shows a schematic of the ring magnet test setup. Results using the equations (24) through (30) are plotted in Fig. 13 along with a Voigt-Thompson model. The easy-axis is by description the natural zero energy orientation state of the magnetization. This orientation is governed by deposition conditions and by geometry. Figure 14 shows a easy-axis curve along with a hard-axis curve. To sort out the below saturation behavior it is necessary to solve (10) for the magnitude of the change in angle for a given resistance.

This rearranging results in (31),

$$|\cos\theta| = \left[\frac{1}{4C}\left[\left[\left[\frac{V_o}{I_s R_o} - A\right]\frac{1}{B}\right]^2 - C^2 - 1 + 2C\right]\right]^{\frac{1}{2}}. \tag{31}$$

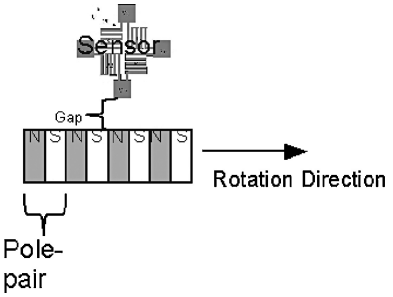

Fig. 12 Schematic of the ring magnet test set up. The field at the sensor is above the saturation field

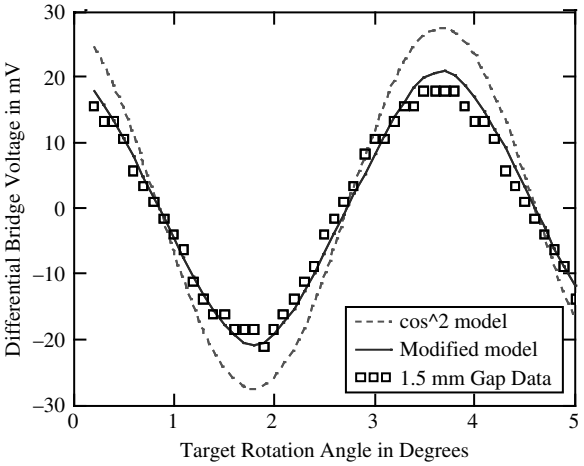

Fig. 13 Comparison of experimental magnetoresistor bridge and the bridge model versus the angle of rotation for a ring magnet on a spindle. The model assumes that the magnetic field saturates the magnetoresistor and the external field rotates 360° every 7.5° of spindle rotation. The $\cos^2\theta$ (Voigt-Kelvin) model over-predicts the sensitivity of the 200° sensor [28, 29]. The gap between the sensor and the ring magnet is 1.5 mm

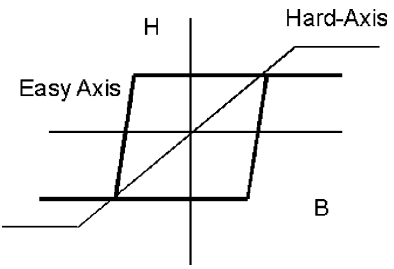

Fig. 14 Hard and easy axis curves for a single domain magnetoresistive films

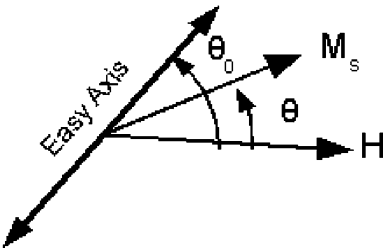

Fig. 15 Domain magnetization rotation off of the easy axis

It is important to relate the change in angle to a given external field. Figure 15 is a schematic of the field rotation vectors.

From Chikazumi and Charap [30] we get,

$$E = -K_u \cos^2(\theta - \theta_o) - M_s H \cos\theta, \tag{32}$$

where E is the energy of the system, K_u is constant of uniaxial anisotropy and M_s is the saturation magnetization. To minimize the energy, the derivative of the energy with the angle of rotation is taken. This derivative is

$$\frac{\mathrm{d}E}{\mathrm{d}\theta} = -K_u \sin 2(\theta - \theta_o) - M_s H \sin\theta. \tag{33}$$

For a weak magnetic field which is $H << K_u/M_s$ and θ_0 is nearly equal to θ then (33) is

$$2K_u \Delta\theta = M_s H \sin\theta_o \tag{34}$$

then

$$\Delta\theta = \frac{M_s H}{2K_u} \sin\theta_o. \tag{35}$$

The modification to match actual off-axis magnetization rotation requires that the geometry of magnetization vector (in the lattice) and the geometry of K_u be considered. If both are initially assumed to be orthorhombic in nature (i.e. rectangular in the 2-d plane) then

$$\Delta\theta = \frac{M}{2K_u} H = \frac{M_o \left[(1 + \alpha\cos 2\theta)^2 + (\alpha \sin 2\theta)\right]^{\frac{1}{2}}}{2K_u \left[(1 + \delta\cos 2\theta)^2 + (\delta \sin 2\theta)\right]^{\frac{1}{2}}} \tag{36}$$

Figures 16 and 17 show the application of (36) to the magnetoresistance equation (20). The results show that we have a reasonable amount of correlation. The sensitivity to the applied field angle for a single strip sensor is fairly high as shown in Fig. 18. Ten degrees of rotation will result in 20% decrease in the positive field direction but a slight increase in the negative field direction. If the resistor is rotated 45°, the sensitivity in the negative field direction is significantly higher than the positive field direction. This holds true until the magnetization reversal happens and then the behavior reverses direction. Figure 19 shows this behavior with sev-

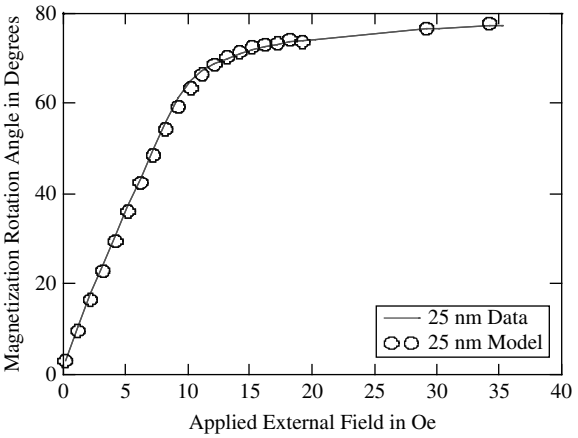

Fig. 16 Hard axis magnetization rotation versus external applied field for an actual 25 nm resistor and a model of a 25 nm resistor. This model is tensor based

eral different resistor widths for a 37.5 nm thick resistor. This behavior is caused by magnetization reversal and can cause problems when using the Permalloy sensor to trigger at a particular field level. Another important effect to consider is the influence of proximity. This proximity effect is due to the below saturation sensitivity increase when two AMR resistors are place in close proximity with each other. This spacing between the adjacent resistors is called the 'gap'. Previously we have shown the effect of changing thickness on the sensitivity of the AMR element but there also is an effect of element width on the sensitivity.

This thickness to width ratio is one measure of the sensitivity while proximity is another measure. As shown in the preceding section the thickness effects both the initial slope and the maximum sensitivity at saturation. Additionally the width of

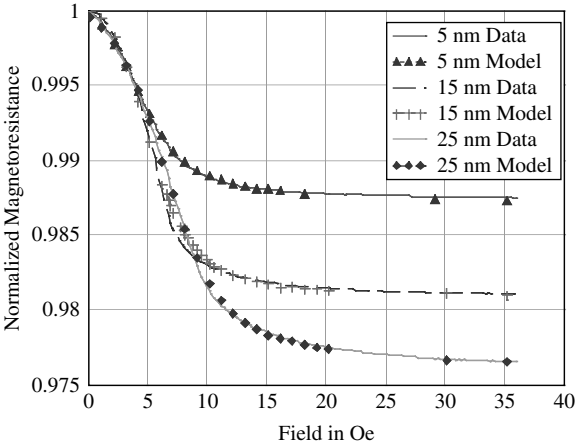

Fig. 17 HA magnetorestance versus applied field for various thickness magnetoresistors with a constant 35 μm width. The tensors used for this model assumes rhombehedral geometry

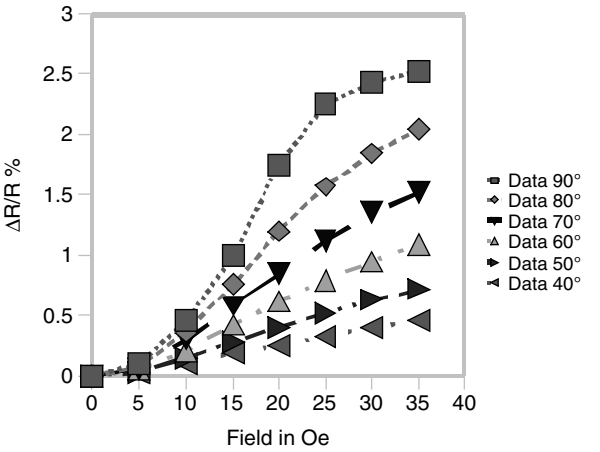

Fig. 18 Effect of field rotation on a single 20μm resistor. This reduction of sensitivity shows the importance of sensor alignment to the external applied field

the resistor for a given resistor thickness can effect the slope but not the maximum sensitivity at saturation. The demagnetizing field is described by Dibbern [22] and also Pant [32] as $H_d \approx (t/w)\, M_s/4\pi$
where t is the film thickness and w is the width of the resistor.

When more than one resistor is placed in close proximity the adjacent resistors tend to influence each other. The closer the spacing between elements the stronger the proximity effect on the elements. Figure 20 is a schematic representation of such a resistor array. Pant [32] defines a scale factor for the adjacency of the resistors with the relationship of spacing 'g' with respect to the resistor width, w. The equation is for the proximity effect, calculated from the electrostatic model, is

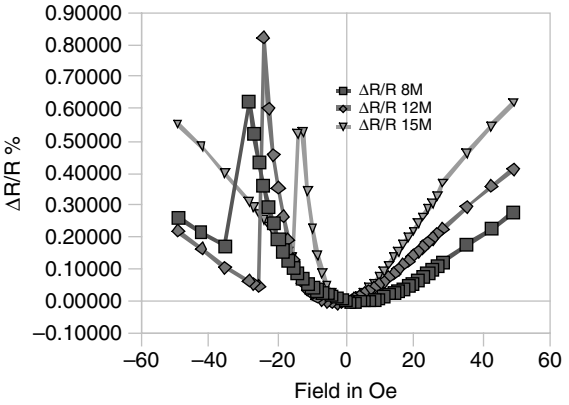

Fig. 19 Single resistor elements of different widths with a 45° applied field

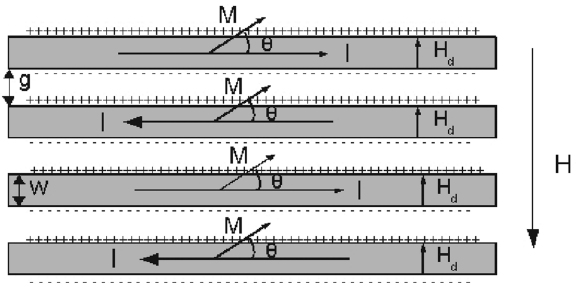

Fig. 20 Schematic of sensor elements using the proximity effect for a serpentine resistor array. The analysis of the effect uses the electrostatic model for magnetics and can be solved numerically [31]

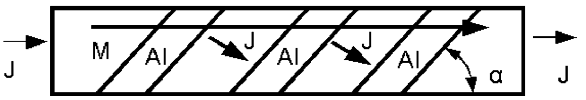

Fig. 21 This figure shows a typical barber-pole sensor element. The angle α and the width of the aluminum shorting straps are determined using finite element methods

$$\alpha(g/w) = \frac{2(g/w)}{1+2g/w} + \frac{g/w}{2(1+g/w)^2}(\pi/2-4) \tag{37}$$

so that

$$H_s \approx H_k + t/w\frac{M_s}{4\pi}\alpha(g/w). \tag{38}$$

Each different resistor width behaves as if it was actually a wider resistor. The easy axis behavior is not affected by proximity so that the hysteresis remains the same as a single element of permalloy. A common method of AMR sensor design is the barber-pole sensor. This sensor manipulates the current orientation versus

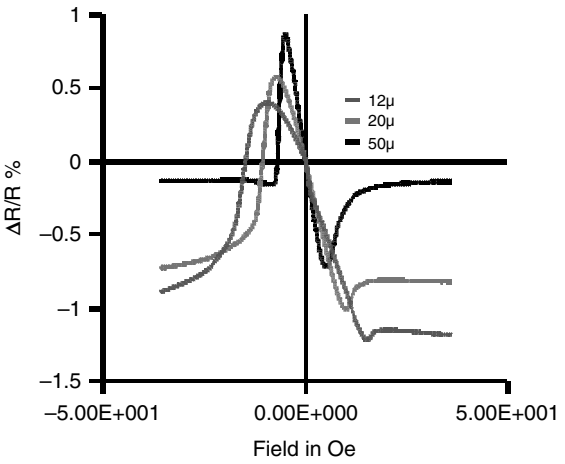

Fig. 22 Response of Barber pole sensor with a 90° applied field

magnetization orientation to create a asymmetrical i.e. odd-function sensor. This odd-function sensor response is completely dependent on the same issues as the single strip element and also is dependent on the orientation of the magnetization orientation at zero applied field. An additional issue with the barber-pole sensor is the element resistance. Since the aluminum shorting straps are significantly lower in resistance then the permalloy, the sensor elements designed using this method are generally much larger than the non barber-pole sensor. Figure 21 shows the important components of the barber-pole sensor. These type of sensors are produced commercially by Philips and Honeywell. The actual design of the shorting straps requires the use of a finite element program such as ANSYS. The models shown in Tummanski [23] for this type of sensor are focused on the linear region of the sensor. It is possible using equation (20), equations (35) and (36) to model the entire sensor behavior. Another complication of this type of sensor is the sense of direction for the magnetization. Both Honeywell and Phillips approach this problem from different directions. In Bharat B. Pants patent [32] the method proposed to keep the magnetization sense is the use of 'high-current' straps.

The data in Fig. 22 is generated for barber pole elements using three different resistor widths with a constant shorting strap design. The offset of the resistor data from the 50 µm and the 20 µm and 12 µm is due to the crowding of the current lines at the edge.

5 Future Progress

The uses of magnetic sensors over the last four decades has continually evolved as manufacturing technology has evolved. The introduction of giant magnetoresistors made from magnetoresistive materials has further increased the applications and scope of the basic effect. The introduction of nano-technology will further increase the use of these materials. Nanostructures for data storage applications and

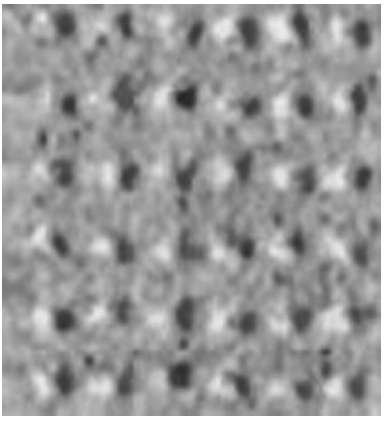

Fig. 23 A MFM image in which the dot magnetizations are organized. Image was produced in air, spacing 1 µm center to center dot size 200 nm. Image obtained using a Quesant Q-Scope 350 MFM with a cobalt tip

possibly for computing applications may well use ferromagnetic materials such as permalloy. Additionally, nanomagnetoresistive structures have been proposed. Work by Kanparthy [34] in Fig. 23 shows the interaction of nanodots using a Magnetic Force Microscope (MFM). The magnetization patterns may be used to store information in hard drives though a more efficient method to write the data to the nanodots must be developed. This behavior at 200 nm is similar to images made by Zhu et al. [35]. Similar structures may be useful for memory or sensing applications. These structures have complex interactions in which the patterns have some meaning but at this point are still in the process of being understood. Zhu et al. [35] have demonstrated the ability to change the magnetic orientation with their MFM tip. Another interesting development in the area of magnetic nanostructures is the study of magnetic properties of permalloy nanowires [36, 37, 38]. Permalloy retains much of its behavior in the nano-scale making it a good candidate for nano-dimensional sensors.

Several different methods for the manufacturing of nanowires have been reported. These are traditional photo-patterning, e-beam lithography, and nano-templating by the use of anodic nanoporous aluminum oxide to form the nano-wires. All these methods have merit and will continue to have importance for the next decade. The future of magnetic sensing, in the nano-scale, may be a material that has been in use since the 1930s.

References

1. R. S. Popovic, Hall Effect Devices, CRC Press, 2004 2nd edition
2. Cohen, Isaac, 'Self aligned hall with field plate', US Patent 7,002,229, February 21, 2006
3. M. Plagens, M. Haji-Sheikh, and W. Matzen, 'Hall-effect element with integrated offset control and method for operating hall-effect element to reduce null offset', US Patent 6,492,697, December 10, 2002.
4. A. Alexander, P. Nickson, and D. Foley, 'Monolithic magnetic sensor having externally adjustable temperature compensation', US patent 6,154,027, November 28, 2000.
5. R. Steiner, A. Haeberli, F. Steiner, and Christoph Maier, 'Spinning current method of reducing the offset voltage of a hall device', US Patent 6,064,202, May 16, 2000.
6. J. Higgs and J. Humenick, 'Integrated circuit with stress isolated Hall element', US Patent 4,578,962, March 25, 1986.
7. A. Bilotti and Gerardo Monreal, 'Chopped hall sensor with synchronously chopped sample-and-hold circuit', US Patent 5,621,319, December 8, 1995.
8. K. Matsuda, Y. Kanda, and K. Suzuki, 'second-order piezoresistance coefficients of *n*-type silicon', Jpn. J. Appl. Phys., 28, L1676–L1677 (1989).
9. Y. Kanda, 'A graphical representation of the piezoresistance coefficients in silicon', IEEE Trans. on Electron Devices, ED-29, 1 , January (1982).
10. D. A. Nepela and R. I. Potter, 'Head assembly for recording and reading, employing inductive and magnetoresistive elements', US patent 3,887,945, June 3, 1975.
11. F. Lee, 'Supersensitive magnetoresistive sensor for high density magnetic read head', US Patent 4,047,236, Sept. 6, 1977.
12. T. McGuire and R. Potter, 'Anisotropic magnetoresistance in ferromagnetic 3d alloys', IEEE Trans. Magn., 11, 4, 1018–1038, (July 1975).

13. K. Kanai, 'Magnetic head with thin sheet exhibiting magnetoresistive property', US Patent 4,051,542, Sept. 27, 1977.
14. K. Kanai, 'High sensitivity magnetic head using magneto-resistive effect element', US Patent 4,068,272, Jan. 10, 1978.
15. J.-P. Lazzari, 'Magnetic transduction device with magnetoresistances', US Patent 4,315,291, Feb. 9, 1982.
16. J.-P. Lazzari, 'Magnetic reading and writing head with magnetoresistant element', US Patent 5,168,408, Dec. 1, 1992.
17. T. A. Schwarz, P. G. Bischoff, C. M. Leung, J. C. Chen, and-P. Thayamballi, 'Method of making a magnetoresistive head with integrated bias and magnetic sheild layer', US Patent 5,312,644, May 17, 1994.
18. M. T. Krounbi, J. H.-T. Lee,'Simplified method of making merged MR head', US Patent 5,779,923, July 14, 1998.
19. M. C. Paul, G. F. Sauter, and P. E. Oberg, 'Thin-Ferromagnetic-Film magnetoresistance manetometer sensitive to easy axis field components and biased to be insensitive to hard axis components', US Patent 3,546,579, Dec. 8, 1970.
20. S. Ito, M. Nagao, K. Toki, and K Morita, 'Magnetic rotary encoder for detection of incremental angular displacement', US Patent 4,319,188, Mar. 9, 1982.
21. M. J. Haji-Sheikh, M. Plagens, and R. Kryzanowski,' Magnetoresistive speed and direction sensing method and apparatus', US Patent 6,784,659, August 31, 2004.
22. U. Dibbern, 'Magnetic field sensors using the magnetoresistive effect', Sensors and Actuators, 10, 127–140, (1986).
23. S. Tummanski, Thin Film Magnetoresistive Sensors, IOP 2001, pp. 19–30.
24. T. Yeh, M. Sivertsen, and C.-L. Lin, ' Preferred Crystal Orientation of NiFe Underlayers and its effect on Magnetostriction of Co/Cu/Co Thin Films', IEEE Trans. on Magn., 34, (4) (July 1998).
25. L. Berger and S. A. Friedberg, 'Magnetoresistance of a permalloy single crystal and effect of 3d orbital degeneracies', Phys. Rev., 165, (2) pp. 670–679, (1968).
26. Th. Rijks and S. Lenczowski, 'In-plane and out of plane magnetoresistance i...', Phys. Rev. B, pp. 362–366, (1997).
27. J. F. Nye, Physical Properties of Crystals, Oxford Science Publications, first publication 1959.
28. M. J. Haji-Sheikh et. al., 'Anisotropic Magnetoresistive Model for ...', IEEE Sens. J., pp. 1258–1263, Dec. 2005.
29. M. J. Haji-Sheikh and Y. Yoo, 'An accurate model of a highly ordered 81/19 Permalloy AMR Wheatstone bridge sensor against a 48 pole pair ring-magnet', IJISTA, 3, No (1/2), 95–105, (2007).
30. S. Chikazumi and S. Charap, Physics of Magnetism, Robert E. Krieger Publishing Company, pp. 260–263, (1978).
31. Michael Haji-Sheikh, 'TaN/NiFe/TaN anisotropic magnetic sensor element', US Patent 5,667,879, September 16, 1997.
32. B.B. Pant, J. Appl. Phys. 79, 6123 (1996).
33. B. B. Pant, D. R. Krahn, and R. B. Fryer, 'Magnetic field sensing device', US Patent 5,247,278, September 21, 1993.
34. S. Kanparthy, Thesis, Northern Illinois University, Fall (2007).
35. X. Zhu , P. Grütter, V. Metlushko, and B. Ilic, 'Magnetic force microscopy study of electron-beam-patterned soft permalloy particles: Technique and magnetization behavior', Phys. Rev. B, 66, 024423, (2002).
36. Y. Rheem, B.-Y. Yoo, B.K. Koo, W.P. Beyermann, and N. V. Myung,'Synthesis and magneto-transport studies of single nickel-rich NiFe nanowire', J. Phys. D: Appl. Phys. 40, 7267–7272, (2007).
37. L. Piraux, K. Renard, R. Guillemet, S. Mtéfi-Tempfli, M. Mtéfi-Tempfli, V. A. Antohe, S. Fusil, K. Bouzehouane, and V. Crosb,'Template-Grown NiFe/Cu/NiFe Nanowires for Spin Transfer Devices', Nano Lett., 7(9), 2563–2567, (2007).
38. A. O. Adeyeye, R. L. White,'Magnetoresistance behavior of single castellated $Ni_{80}Fe_{20}$ nanowires', J. Appl. Phys. 95, 2025 (2004).

http://www.springer.com/978-3-540-69030-6

Sensors
Advancements in Modeling, Design Issues, Fabrication and Practical Applications
Huang, Y.-M. (Ed.)
2008, XX, 424 p. 611 illus., Hardcover
ISBN: 978-3-540-69030-6